JOURNAL OF MATERIALS SCIENCE 31 (1996) 272–279

Porosity-dependence of ultrasonic velocity in sintered materials – a model based on the self-consistent spheroidal inclusion theory

K. K. PHANI
Central Glass and Ceramic Research Institute, Calcutta 700 032, India

The porosity dependence of ultrasonic velocity in porous sintered materials has been modelled using the self-consistent spheroidal inclusion theory. Considering the pores to be oblate spheroids, an effective aspect ratio has been determined from experimental data, which serves as an additional parameter to describe the observed variation in ultrasonic velocity with porosity. With the exception of two cases in the ten investigated, this single parameter describes satisfactorily the variation of both longitudinal ultrasonic velocity and transverse ultrasonic velocity with volume fraction of pores.

1. Introduction

The ultrasonic velocity measurement method provides a useful and convenient non-destructive technique for estimating the porosity fraction in polycrystalline materials and has been the subject of several experimental investigations [1–12]. Theoretically, the porosity-dependence of ultrasonic velocity can be derived from the theories dealing with the elastic properties of porous material utilizing the velocity–elastic property relations given by physical acoustics theory. In addition, theories based on acoustic scattering [13–16] for ultrasonic velocity variation in two-phase composites can also be used to derive such relations considering one of the phases to be pores. However, the comparison between experiment and theory has not received much attention in the literature. To the author's knowledge, the only such application of theories to experimental data has been the work of Panakkal *et al.* [11, 12], who compared the observed variations of the ultrasonic velocities in sintered clay ceramics and powder iron compacts with the theoretical predictions of both elasticity and scattering theories. Large deviations were observed from the theoretically predicted values and this was attributed to the non-spherical shape of the pores, because the theories used were based on spherical pores. They suggested that a more rigorous model which took into account the non-spherical nature of the pores would be able to explain the experimental data better.

In a recent review [17], Roth *et al.* analysed the experimental data on ultrasonic velocity versus porosity for various porous sintered materials. Their analysis showed that the experimental data for both longitudinal ultrasonic velocity and transverse ultrasonic velocity tend to vary linearly with porosity, and the slopes of the fitted equations varied with the material. Even the slope for what was believed to be the same material varied for different investigations. One of the factors suggested to account for these variations was pore-size distribution and its geometry.

This paper presents a comparison between theory and experiment based on the self-consistent spheroidal theory to determine the importance of pore-geometry factor as an additional parameter to describe ultrasonic velocity versus porosity data on sintered materials.

2. Theory

A brief review of various theories based on the self-consistent scheme was given by Dean [18]. In the self-consistent spheroidal inclusion theory, the inclusion is considered as spheroids and characterized by the aspect ratio, α, which is defined as the ratio of the minor axis to the major axis. For $\alpha = 1$ spheroids become spheres and as α approaches zero, oblate spheroids become disc-shaped and prolate spheroids become needle-shaped. Dean [18] used the self-consistent spheroidal theory given by Wu [19] to analyse the elastic moduli versus porosity data on sintered materials. Considering the pores to be oblate spheroids and using an effective aspect ratio as the single variable parameter, he obtained excellent agreement between the theory and experiment for six cases out of seven investigated. The same procedure is adopted here to analyse ultrasonic velocity versus porosity data.

The analysis is based on the following assumptions

(1) Pores are oblate spheroids and are randomly oriented so that on a macroscopic scale the material behaviour is isotropic.

(2) A batch of sintered materials with individual members having large ranges of porosities may have pores with aspect ratio of individual pores varying over the range 0 to 1, but their effect on ultrasonic velocity can be approximated by a material having

0022–2461

same volume fraction of pores with individual pores having identical aspect ratio. This single aspect ratio is defined as the "effective" aspect ratio which approximates the result of a spectrum of aspect ratios.

The validity of this second assumption has already been shown by Dean [18] for elastic moduli–porosity relation. The same treatment can be used to show that it is valid for ultrasonic velocity also. Based on the above assumptions and considering the bulk modulus of air in the pores as negligible, the effective bulk modulus, K, and the effective shear modulus, G, of a porous body having a volume fraction of porosity, ϕ, is given by Wu's [19] theory as

$$K = K_0[1 - \phi P_0(\alpha, R)] \quad (1)$$

$$G = G_0[1 - \phi Q_0(\alpha, R)] \quad (2)$$

where K_0 and G_0 are the bulk modulus and the shear modulus of pore-free material respectively; P_0 and Q_0 are functions of the effective aspect ratio α of spheroids, and R, defined as

$$R = 3G/(3K + 4G) \quad (3)$$

The functions P_0 and Q_0 for oblate spheroidal pores are given in Appendix 1.

Longitudinal ultrasonic velocity, V_1, and transverse ultrasonic velocity, V_s, are related to K and G by the relations

$$V_1 = [(K + 4/3G)/\rho]^{1/2} \quad (4)$$

$$V_s = [G/\rho]^{1/2} \quad (5)$$

where ρ is the density of the material. ρ is related to the density of pore-free material, ρ_0, by the relation

$$\rho = \rho_0(1 - \phi) \quad (6)$$

Substitution of Equations 4 and 5 into Equation 3 along with Equations 1 and 2 gives the relation

$$3RV_{10}^2[1 - \phi P_0(\alpha, R)] + V_{s0}^2[4\phi R P_0(\alpha, R) - \phi(4R - 3)Q_0(\alpha, R) - 3] = 0 \quad (7)$$

where the subscript 0 refers to pore-free material. Further substitution of the relation

$$(v_{10}/v_{s0})^2 = \frac{2(\nu_0 - 1)}{(2\nu_0 - 1)} \quad (8)$$

in Equation 7 leads to the relation

$$6R(\nu_0 - 1)[1 - \phi P_0(\alpha, R)] + (2\nu_0 - 1)[4\phi R P_0(\alpha, R) - \phi(4R - 3)Q_0(\alpha, R) - 3] \quad (9)$$

For particular values of ν_0 and α, Equation 9 is a fifth degree equation in R. However, for spheres, i.e. $\alpha = 1$, the equation reduces to a quadratic one which can be solved explicitly. A computer program has been run to solve the equation by the Newton–Raphson method. Once R has been determined, values of P_0 and Q_0 follow from the relations given in Appendix 1 and the velocity values V_1 and V_s as a function of ϕ are obtained from Equations 4 and 5 using Equations 1 and 2.

3. Fitting experimental data to the theory

To obtain the value of the effective spheroid aspect ratio which fits both the measured longitudinal velocity and transverse velocity versus porosity data, the least square method suggested by Dean [18] was adopted. Numerical solutions of Equations 4 and 5 for longitudinal and transverse velocity versus porosity over large ranges of Poisson's ratio of pore-free material and spheroid aspect ratio show that both these velocity–porosity relations have noticeable curvature. Thus the theoretical results were fitted to the relations

$$V_1 = V_{10}[1 - \phi e(\alpha, \nu_0) - \phi^2 f(\alpha, \nu_0)] \quad (10)$$

$$V_s = V_{s0}[1 - \phi g(\alpha, \nu_0) - \phi^2 h(\alpha, \nu_0)] \quad (11)$$

where the functions e, f, g and h are least-square fit to the velocity values determined from Equations 4 and 5 for various values of the effective aspect ratio, α, and Poisson's ratio, ν_0. The basis for choosing second-degree poynomials for both the equations is that Dean's [18] analysis indicates that variation of effective Young's and shear moduli with porosity follow a linear and a second-degree polynomial equation, respectively. Combining these equations with Equations 4 and 5 and neglecting the terms of higher order than ϕ^2, leads to Equations 10 and 11.

Each of the least-squares coefficients e, f, g and h was calculated for values of $\alpha = 0.001, 0.05, 0.1, \ldots, 0.95, 1$, and $\nu_0 = 0.14, 0.16, \ldots, 0.34, 0.36$. In all cases the regression coefficient was better than 0.998. A polynomial least-squares fit of the form

$$e(\alpha, \nu_0) = e_1(\nu_0)/\alpha + e_2(\nu_0) + \alpha e_3(\nu_0) + \alpha^2 e_4(\nu_0) \quad (12)$$

with a similar fit for $f(\alpha, \nu_0)$, $g(\alpha, \nu_0)$ and $h(\alpha, \nu_0)$, described the variation in α with regression coefficient better than 0.980 in each case. Finally the functions $e_i(\nu_0)$, $f_i(\nu_0)$, $g_i(\nu_0)$ and $h_i(\nu_0)$ were fitted quadratically to the variation in ν_0 with regression coefficient better than 0.990 in each case. The values of these coefficients are given in Appendix 2.

Using Equations 10 and 11 as the fitting equations for the experimental data, it follows

$$y_i = (V_{10} - V_{1i})/\phi_i V_{10} = e(\alpha, \nu_0) + \phi_i f(\alpha, \nu_0) \quad (13)$$

$$z_i = (V_{s0} - V_{si})/\phi_i V_{s0} = g(\alpha, \nu_0) + \phi_i h(\alpha, \nu_0) \quad (14)$$

where $i = 1, 2, \ldots, n$ is the number of data. The function to be minimized is the sum of squares of the residues of Equations 13 and 14, i.e.

$$S = \sum_{i=1}^{n} (y_i - e - \phi_i f)^2 + \sum_{i=1}^{n} (z_i - g - \phi_i h)^2 \quad (15)$$

$\partial S/\partial\alpha = 0$ gives the condition equation as

$$\left[\sum y - ne - f\sum\phi\right]\frac{\partial e}{\partial\alpha} + \left[\sum\phi y - e\sum\phi - f\sum\phi^2\right]\frac{\partial f}{\partial\alpha} + \left[\sum z - ng - h\sum\phi\right]\frac{\partial g}{\partial\alpha} + \left[\sum\phi z - g\sum\phi - h\sum\phi^2\right]\frac{\partial h}{\partial\alpha} = 0 \quad (16)$$

where the summation is taken over $i = 1$ to n. Equation 16 is a sixth-degree equation in α and it is solved by the Newton–Raphson method. This method of finding the best value of aspect ratio to fit both longitudinal and transverse velocity data was used on seven groups of data. The results are given in the next section.

4. Results

This section presents the analysis of seven data groups. Among these, six groups were taken from the twelve groups of data analysed by Roth *et al.* [17]. These include one set each for SiC, Al_2O_3, $YBa_2Cu_3O_{7-x}$, porcelain; two sets for Si_3N_4, and three sets for tungsten. One more set for sintered iron powder compacts was taken from the literature [11]. Only those data sets for which sufficient data were available over a reasonably wide porosity range were selected for this analysis. The data sets were fitted by the method described above to find the best aspect ratio for oblate spheroidal theory. The velocity values for pore-free material were estimated from single-crystal constants. Unfortunately, except for Al_2O_3, single-crystal constants for none of the materials analysed here were available. For these cases, velocity values of pore-free material obtained by Roth *et al.* [17] by regression analysis of data, were used.

4.1. SiC

Experimental data on SiC reported by Baaklini *et al.* [6] are shown in Fig. 1. The data were read from the plot given in their paper. This was the only set of data for which information about mean pore size and shape was available. However, the data were available for longitudinal velocity only. So Equation 16 was minimized for longitudinal velocity only using $V_{l0} = 1.21\ \text{cm}\,\mu\text{s}^{-1}$. The solution of the self-consistent oblate spheroidal theory with $\alpha = 0.262$ is also shown in Fig. 1. Although the polynomial fit to the theory was used to find the best-fit value of α, the curve shown was calculated using the implicit formulas, Equations 4 and 5. The theory agrees with the data extremely well. The low value of $\alpha = 0.262$ indicates that the pores are more disc-shaped than needle-shaped. This agrees well with the pore shape reported by the authors, which is also shown in Fig. 1 for one batch of samples.

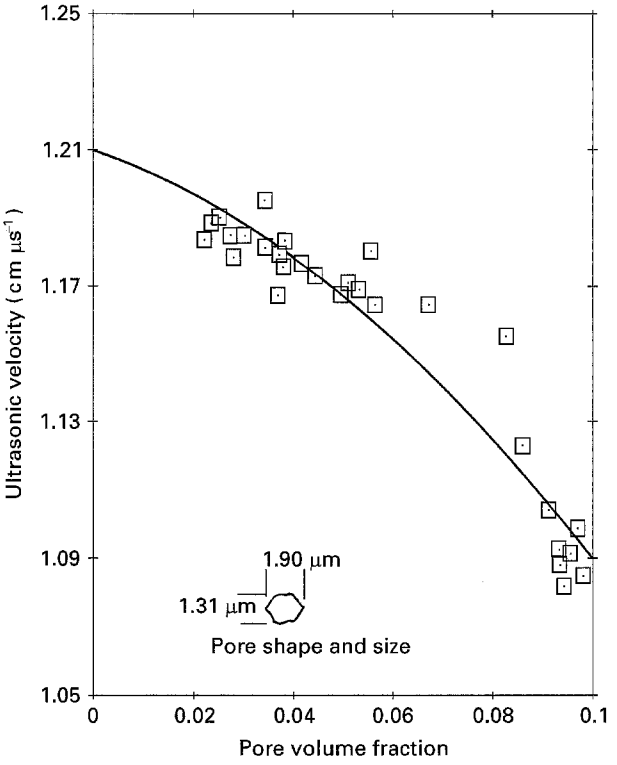

Figure 1 SiC data from Baaklini *et al.* [6]; constants for theoretical curve $V_{l0} = 1.21\ \text{cm}\,\mu\text{s}^{-1}$ and $\alpha = 0.262$. (⊡) Longitudinal.

4.2. Si_3N_4

Experimental data on hot-pressed Si_3N_4 by McLean *et al.* are shown in Fig. 2. The data were taken from the report of Roth *et al.* [17]. The theoretical calculations were based on $V_{l0} = 0.977\ \text{cm}\,\mu\text{s}^{-1}$ and $V_{s0} = 0.585\ \text{cm}\,\mu\text{s}^{-1}$. These values were calculated by Roth *et al.* [17] (Table II in [17]) from the values of elastic moduli of fully dense polycrystalline material. The aspect ratio for the theoretical curves shown in Fig. 2 is $\alpha = 0.441$. The experimental data agree well with the theory.

The second group of data obtained by Thorp and Bushell [7] for reaction-bonded Si_3N_4 are shown in Fig. 3. The theoretical calculations were again based on velocity values given above. The aspect ratio for the theoretical curves shown in Fig. 3 is $\alpha = 0.621$. Here the experimental data are in total agreement with the theory.

The values of aspect ratio of 0.441 and 0.621 indicate that the pore shape is more tilted towards spherical than disc-shaped

4.3. Al_2O_3

Fig. 4 shows the experimental data on Al_2O_3 reported by Nagarajan [2]. The velocity values of pore-free material were taken as $V_{l0} = 1.11\ \text{cm}\,\mu\text{s}^{-1}$ and $V_{s0} = 0.64\ \text{cm}\,\mu\text{s}^{-1}$ for theoretical calculations. These values were calculated from the mean polycrystalline (VRH) values for $K_0 = 251.0$ GPa and $G_0 = 162.9$ GPa reported by Anderson *et al.* [20]. The best fit was obtained for $\alpha = 0.572$, which is also shown in Fig. 4. In this case the theory fails to explain the experimental data, especially the longitudinal velocity for which the deviations from the theory at

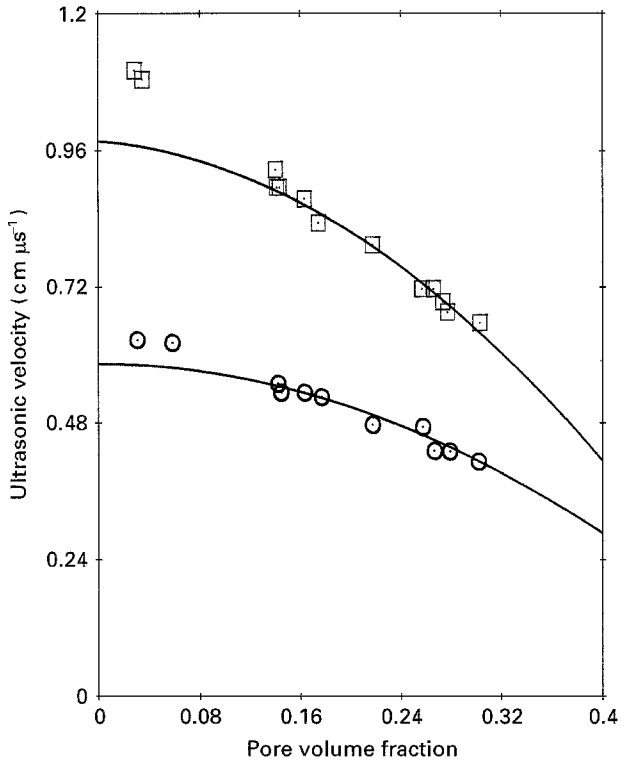

Figure 2 Hot-pressed Si_3Ni_4 data from Roth *et al.* [17]; constants for theoretical curves $V_{l0} = 0.977\ cm\ \mu s^{-1}$, $v_{s0} = 0.585\ cm\ \mu s^{-1}$ and $\alpha = 0.441$. (⊡) Longitudinal (⊙) transverse.

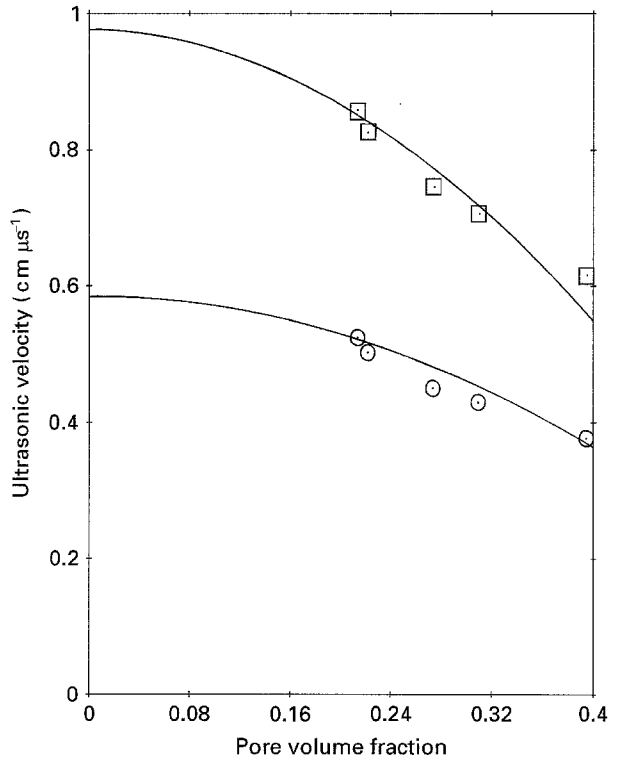

Figure 3 Reaction-bonded Si_3N_4 data from Roth *et al.* [7]; constants used for theoretical curves are the same as for Fig. 2, and the aspect ratio $\alpha = 0.621$. (⊡) Longitudinal, (⊙) transverse.

low porosities are more than 10%. Nagarajan [2] compared the elastic moduli values calculated from the measured ultrasonic velocities with the models based on elastic-bounds and concluded that a model based on the cylindrical pore with the pores orientated

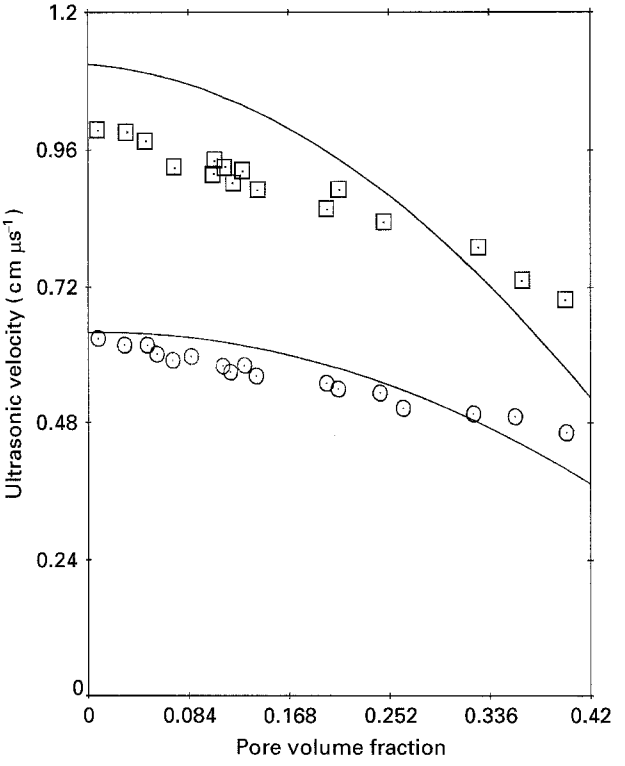

Figure 4 Al_2O_3 data from Nagarajan [2]; constants for theoretical curves $v_{l0} = 1.11\ cm\ \mu s^{-1}$, $v_{s0} = 0.64\ cm\ \mu s^{-1}$ and $\alpha = 0.572$. (⊡) Longitudinal, (⊙) transverse.

perpendicular to the stress described his data better. Thus the difference in the pore-structure model may be the cause of failure of the theory in the present case.

4.4. $YBa_2Cu_3O_{7-x}$

Experimental data on $YBa_2Cu_3O_{7-x}$ by Roth *et al.* [21] are shown in Fig. 5. The shear velocity value has been reported only for a single porosity. The figure also shows five other data points of shear velocity taken from other sources [22–25]. However, they have not been included in the regression analysis. The theoretical calculations were based on the values of $V_{l0} = 0.565\ cm\ \mu s^{-1}$ and $V_{s0} = 0.313\ cm\ \mu s^{-1}$ of theoretically dense material. These values were taken from Roth *et al.* (Table II in [17]). The theoretical curves are for an aspect ratio $\alpha = 0.357$. The theory shows excellent agreement with the experimental data. It may be noted that the shear velocity values reported by other researchers [22, 23, 25], though not included in the regression analysis, also show good agreement with the theory, except for that reported by Round and Bridge [24].

4.5. Porcelain

Fig. 6 shows another set of data which the oblate spheroidal theory fails to explain. These data on porcelain were reported by Boisson *et al.* [10]. The velocity values of $V_{l0} = 0.728\ cm\ \mu s^{-1}$ and $V_{s0} = 0.448\ cm\ \mu s^{-1}$ reported by Roth *et al.* [17] were used in the analysis. The best-fit theoretical curve shown in the figure corresponds to $\alpha = 0.294$. Because no information on the pore structure of the material is

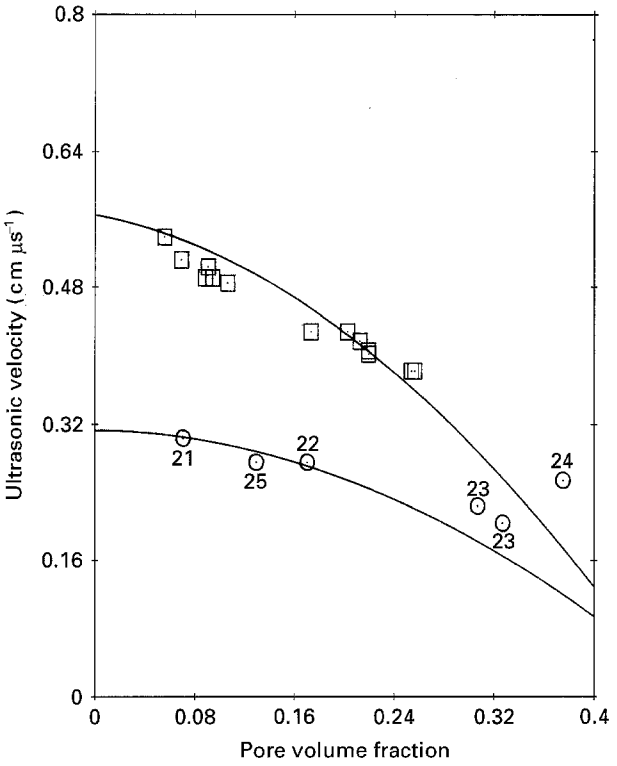

Figure 5 $YBa_2Cu_3O_{7-x}$ data from Roth *et al.* [21]; constants for theoretical curves $v_{l0} = 0.565\ cm\ \mu s^{-1}$, $v_{s0} = 0.313\ cm\ \mu s^{-1}$ and $\alpha = 0.357$. (⊡) Longitudinal, (⊙) transverse.

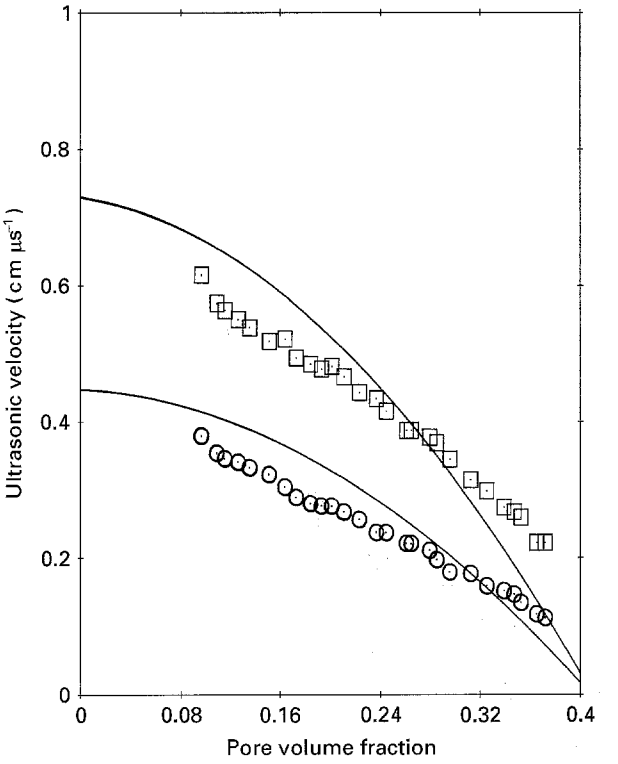

Figure 6 Data on porcelain from Boisson *et al.* [10]; constants for theoretical curves $v_{l0} = 0.728\ cm\ \mu s^{-1}$, $v_{so} = 0.448\ cm\ \mu s^{-1}$ and $\alpha = 0.294$. (⊡) Longitudinal, (⊙) transverse.

available, no suitable explanation can be offered for the failure of the theory.

4.6. Tungsten

Figs 7 and 8 show three data sets on tungsten by Smith and Lopilato [1]. Only the longitudinal

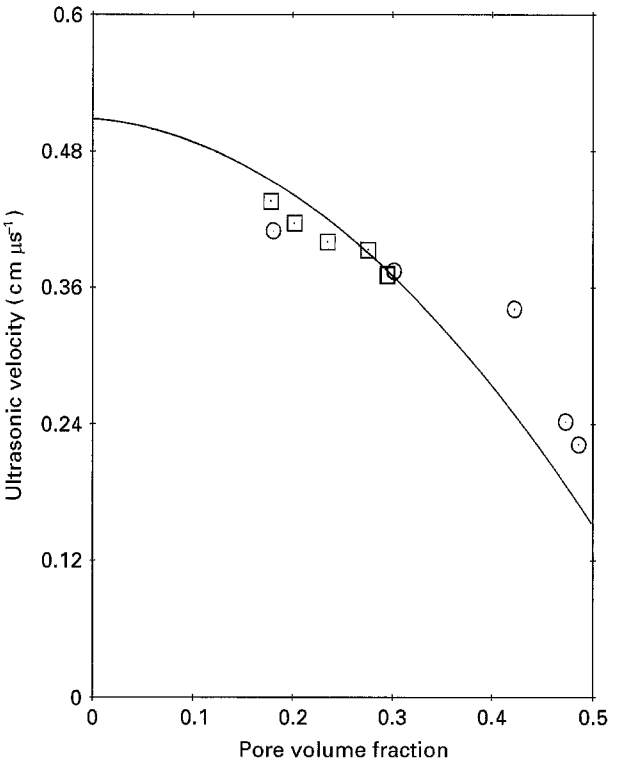

Figure 7 Data on tungsten (initial particle size 4 μm) from Smith and Lopilato [1]; constants for theoretical curves $v_{l0} = 0.509\ cm\ \mu s^{-1}$ and $\alpha = 0.725$. (⊡) Kenna, (⊙) General Electric.

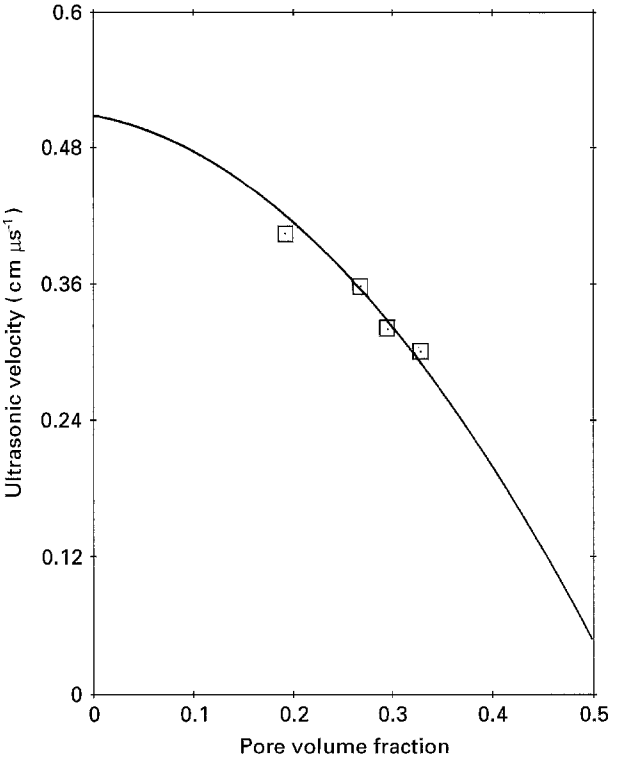

Figure 8 Data on Tungsten (initial particle size 18 μm) from Smith and Lopilato [1]; constant used for the theoretical curve is the same as for Fig. 7 and $\alpha = 0.453$. (⊡) Longitudinal.

velocity values were reported. Two sets shown in Fig. 7 had the same starting powder size of 4 μm, but were from a different source, while the set shown in Fig. 8 had a starting powder size of 18 μm. Theoretical

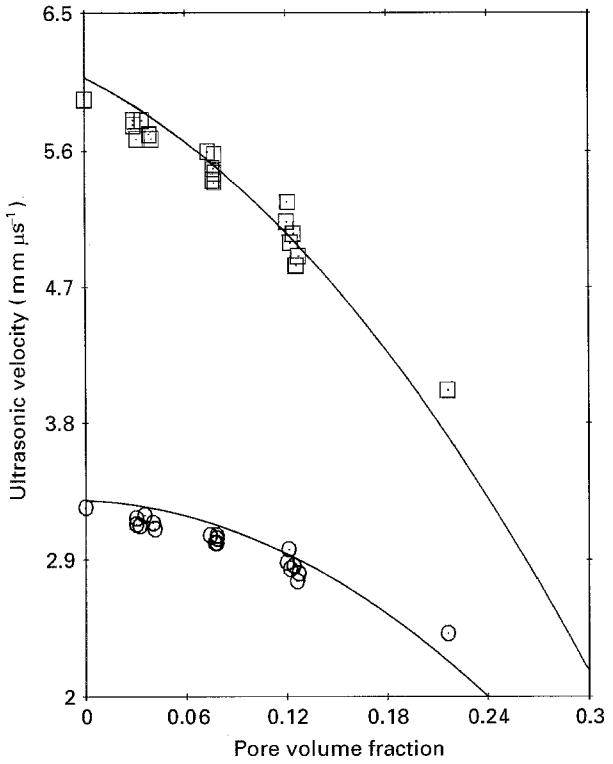

Figure 9 Data on sintered iron powder compacts from Panakkal *et al.* [11]; constants for the theoretical curves $v_{l0} = 6.08\ \text{mm}\,\mu\text{s}^{-1}$, $v_{s0} = 3.29\ \text{mm}\,\mu\text{s}^{-1}$ and $\alpha = 0.273$. (⊡) Longitudinal, (⊙) transverse.

analysis of individual sets gave similar values of aspect ratio for the sets with 4 μm starting powder size, so they were combined together. Theoretical analysis based on $V_{l0} = 0.509\ \text{cm}\,\mu\text{s}^{-1}$ yielded best-fit aspect ratios of 0.725 and 0.453 for 4 and 18 μm starting powder size, respectively. Theoretical curves corresponding to these aspect ratios are also shown in the respective figures. For 18 μm starting powder size the theory shows excellent agreement with the data. With the exception of the 42% porosity velocity value, the data for 4 μm starting powder size agree well with the theory. The aspect ratio of 0.725 for 4 μm starting powder size is almost twice that for the 18 μm powder size, indicating that the pores in these specimens are closer to spherical shape than those of 18 μm powder size specimens.

4.7. Sintered iron powder compacts

The data on sintered iron powder compacts reported by Panakkal *et al.* [11] are shown in Fig. 9. The theoretical calculations were based on $V_{l0} = 6.08\ \text{mm}\,\mu\text{s}^{-1}$ and $V_{s0} = 3.29\ \text{mm}\,\mu\text{s}^{-1}$. These values were calculated from the moduli values of electrolytic iron of $E_0 = 212.0$ GPa and $G_0 = 82.0$ GPa [11]. The theoretical curves shown in the figure correspond to an aspect ratio of 0.273. Here, again the experimental data agree well with the theory.

5. Discussion

Of the ten sets of data analysed, only two sets of data could not be fitted by the self-consistent oblate spheroidal theory. It may be recalled that the only adjustable parameter used in this analysis is the aspect ratio of pores, thus establishing pore geometry as one of the major factors affecting ultrasonic velocity in porous material. Out of the two sets of data which remained unexplained, the one on Al_2O_3 may again possibly be explained based on a model different from that used here for pore geometry and orientation. However, for the other unexplained data on porcelain, a similar conclusion cannot be drawn in absence of microstructural details.

It may be noted that the values of effective aspect ratio obtained for different materials varied over the range 0.262 to 0.725. The minimum of 0.262 was obtained for SiC indicating disc-shaped pores and the maximum of 0.725 for tungsten indicating the pores to be of sphere-like shape. However, from this, no conclusion can be drawn whether any relation exists between the effective aspect ratio and the process of fabrication or the final product, except for the hint that it may be dependent on initial particle size as shown by the results of two different starting powder sizes of tungsten or on the process of sintering as shown by the results of hot-pressed and reaction-bonded silicon nitride.

6. Conclusion

The porosity dependence of ultrasonic velocity in sintered materials has been modelled based on the self-consistent oblate spheroidal theory. Ten sets of data reported in the literature have been analysed based on this theory. With the exception of the data on Al_2O_3 and porcelain, the ultrasonic velocity of porous sintered marterials is satisfactorily modelled by oblate spheroidal pores with various sintering processes yielding different aspect ratios for the spheroids. Data analysis of the results indicate that the pore geometry is the major factor affecting the ultrasonic velocity in porous materials.

Acknowledgements

The author thanks Dr B. K. Sarkar, Director of the Institute for his kind permission to publish this paper, and Dr D. J. Roth, NASA Lewis Research Centre, for providing some of the data used.

Appendix 1

The functions $P_0(\alpha, R)$ and $Q_0(\alpha, R)$ for the oblate spheroidal pores are given by

$$P_0(\alpha, R) = F_1/F_2 \quad \text{(A1)}$$

$$Q_0(\alpha, R) = \frac{1}{5}\left[\frac{2}{F_3} + \frac{1}{F_4} + \frac{F_5F_4 + F_6F_7 - F_8F_9}{F_2F_4}\right] \quad \text{(A2)}$$

where

$$F_1 = 1 - \tfrac{3}{2}(f + \theta) + R(\tfrac{3}{2}f + \tfrac{5}{2}\theta - \tfrac{4}{3}) \quad \text{(A3)}$$

$$F_2 = R[2\theta - 2f - 3\theta^2 + 2R(f - \theta + 2\theta^2)] \quad \text{(A4)}$$

$$F_3 = f + \tfrac{3}{2}\theta - R(f + \theta) \quad \text{(A5)}$$

$$F_4 = 1 - \tfrac{1}{4}[f + 3\theta - R(f - \theta)] \quad \text{(A6)}$$

$$F_5 = f - R(f + \theta - \tfrac{4}{3}) \quad \text{(A7)}$$

$$F_6 = -f + R(f + \theta) \quad \text{(A8)}$$

$$F_7 = 2 - \tfrac{1}{4}[3f + 9\theta - R(3f + 5\theta)] \quad \text{(A9)}$$

$$F_8 = -1 + \tfrac{1}{2}f + \tfrac{3}{2}\theta + R(2 - \tfrac{1}{2}f - \tfrac{5}{2}\theta) \quad \text{(A10)}$$

$$F_9 = f - R(f - \theta) \quad \text{(A11)}$$

The functions θ and f are given by

$$\theta = \frac{\alpha}{(1 - \alpha^2)^{3/2}}[\cos^{-1}\alpha - \alpha(1 - \alpha^2)^{1/2}] \quad \text{(A12)}$$

$$f = \frac{\alpha^2(3\theta - 2)}{1 - \alpha^2} \quad \text{(A13)}$$

For $\alpha = 1$, Equations A12 and A13 are indeterminate. L'Hospital's rule yields $\theta(1) = 2/3$ and $f(1) = -2/5$ and the corresponding values for P_0 and Q_0 as

$$P_0(1, R) = 3/4R \quad \text{(A14)}$$

$$Q_0/(1, R) = 15/(9 - 4R) \quad \text{(A15)}$$

Substitution of these equations into Equation 9 results in a quadratic in R. Thus there exists an explicit solution of Equation 9 for spherical voids and it is given by

$$R = a - (a^2 - b)^{1/2} \quad \text{(A16)}$$

where

$$a = \frac{[13\nu_0 - 11 - (21\nu_0 - 9)\phi]}{8(\nu_0 - 1)} \quad \text{(A17)}$$

$$b = \frac{3[12\nu_0 - 6 - (23\nu_0 - 7)\phi]}{16(\nu_0 - 1)} \quad \text{(A18)}$$

Once R has been determined, P_0 and Q_0 follow from Equations A14 and A15, and the velocities are given by

$$V_s/V_{s0} = \left[\frac{(1 - \phi Q_0)}{1 - \phi}\right]^{1/2} \quad \text{(A19)}$$

$$V_l/V_{l0} = \left[\frac{2(\nu_0 - 1)}{2(\nu_0 - 1)R}\right]^{1/2}\left(\frac{V_s}{V_{s0}}\right) \quad \text{(A20)}$$

Appendix 2

$$V_l = V_{l0}[1 - \phi e(\alpha, R) - \phi^2 f(\alpha, R)] \quad \text{(A21)}$$

$$V_s = V_{s0}[1 - \phi g(\alpha, R) - \phi^2 h(\alpha, R)] \quad \text{(A22)}$$

where each of functions e, f, g and h are given as

$$e(\alpha, R) = e_1(\nu_0)/\alpha + e_2 + \alpha e_3(\nu_0) + \alpha^2 e_4 \quad \text{(A23)}$$

and the variation with respect to ν_0 is given in terms of $\sigma = \nu_0 - 0.25$ as follows

$$\begin{bmatrix} e_1 \\ e_2 \\ e_3 \\ e_4 \end{bmatrix} = \begin{bmatrix} 0.2556 & 0.8671 & 3.5761 \\ -0.2516 & 1.5425 & 6.9485 \\ -0.3159 & -0.4111 & -1.3444 \\ 0.4081 & 0.5865 & 5.8212 \end{bmatrix} \times \begin{bmatrix} 1 \\ \sigma \\ \sigma^2 \end{bmatrix} \quad \text{(A24)}$$

$$\begin{bmatrix} f_1 \\ f_2 \\ f_3 \\ f_4 \end{bmatrix} = \begin{bmatrix} 1.4783 & -8.3878 & -37.4133 \\ -0.6629 & 19.2815 & 85.8815 \\ -0.2368 & 2.3142 & 10.2054 \\ 2.6021 & -21.4989 & -108.8020 \end{bmatrix} \times \begin{bmatrix} 1 \\ \sigma \\ \sigma^2 \end{bmatrix} \quad \text{(A25)}$$

$$\begin{bmatrix} g_1 \\ g_2 \\ g_3 \\ g_4 \end{bmatrix} = \begin{bmatrix} 0.1321 & -0.1881 & -0.0714 \\ -0.2503 & -0.5796 & -0.9041 \\ -0.2253 & 0.0616 & 0.0059 \\ 0.3541 & 0.1543 & 0.6494 \end{bmatrix} \times \begin{bmatrix} 1 \\ \sigma \\ \sigma^2 \end{bmatrix} \quad \text{(A26)}$$

$$\begin{bmatrix} h_1 \\ h_2 \\ h_3 \\ h_4 \end{bmatrix} = \begin{bmatrix} 2.5045 & 1.7706 & -0.2572 \\ -3.3372 & -3.5701 & -1.1134 \\ -0.5338 & -0.4318 & -0.7178 \\ 5.2192 & 3.8533 & -0.2725 \end{bmatrix} \times \begin{bmatrix} 1 \\ \sigma \\ \sigma^2 \end{bmatrix} \quad \text{(A27)}$$

References

1. J. T. SMITH and S. A. LOPILATO, *Trans. Metall. Soc. AMIE* **236** (1966) 597.
2. A. NAGARAJAN, *J. Appl. Phys.* **42** (1971) 3693.
3. R. M. ARONS and D. S. KUPPERMAN, *Mater. Eval.* **40** (1982) 1076.
4. T. N. CLAYTOR, H. M. FROST, T. H. FEIRTAG, G. A. SHEPPARD and P. D. SHALEK, *ibid.* **47** (1989) 532.
5. D. S. KUPPERMAN and H. B. KARPLUS, *Am. Ceram. Soc. Bull.* **63** (1984) 1505.
6. G. Y. BAAKLINI, E. R. GENERAZIO and J. D. KISER, *Am. Ceram. Soc.* **72** (1989) 383.
7. J. S. THORP and T. G. BUSHELL, *J. Mater. Sci.* **20** (1985) 2265.
8. E. P. PAPADAKIS and B. W. PETERSEN, *Mater. Eval.* **37** (1979) 76.
9. J. P. PANAKKAL and J. K. GHOSH, *J. Mater. Sci. Lett.* **3** (1984) 835.

10. J. BOISSON, F. PLATON and P. BOCH, *Ceramurgia* **6** (1976) 74.
11. J. P. PANAKKAL, H. WILLEMS and W. ARNOLD, *J. Mater. Sci.* **25** (1990) 1397.
12. J. P. PANAKKAL, *Br. J. NDT* **34** (1992) 529.
13. J. G. BERRYMAN, *J. Acoust. Soc. Am.* **68** (1980) 1809.
14. *Idem., ibid.* **68** (1980) 1820.
15. R. H. LATIFF and N. F. FLORE, *ibid.* **57** (1976) 1441.
16. C. M. SAYERS and R. L. SMITH, *Ultrasonics* **19** (1982) 201.
17. D. J. ROTH, D. B. STANG, S. M. SWICKARD and M. R. DeGUIRE, NASA Technical Memorandum 102501, July 1990.
18. E. A. DEAN, *J. Am. Ceram. Soc.* **66** (1983) 847.
19. T. T. WU, *Int. J. Solids Struct.* **3** (1966) 3.
20. O. L. ANDERSON, E. SCHREIBER, R. C. LIEBERMAN and N. SOGA, *Rev. Geophys.* **6** (1968) 491.
21. D. J. ROTH, L. E. DOLHERT and D. P. KERWIN, unpublished Research, NASA Lewis Research Centre, Cleveland, OH (1990).
22. A. L. GAIDUK, S. V. ZHERLITSYN, O. R. PRIKHOD'KO, V. P. SEMINOZHENKO, V. F. NESTERENKO and S. A. PERSHIN, *Sov. J. Low Temp. Phys.* **14** (1988) 395.
23. H. M. LEDBETTER, M. W. AUSTIN, S. A. KIM and M. LEI, *J. Mater. Res.* **2** (1987) 786.
24. R. ROUND and B. BRIDGE, *J. Mater. Sci. Lett.* **6** (1987) 1471.
25. J. E. BLENDELL, C. K. CHIANG, D. C. CRANMER, S. W. FREIMAN, E. R. FULLER Jr, E. DRESCHER-KRASICKA, W. L. JOHNSON, H. M. LEDBETTER, L. H. BENNETT, L. J. SWARTZENDRIBER, R. B. MARINENKO, R. L. MYKLEBUST, D. S. BRIGHT and D. E. NEWBURY, *Ad. Ceram. Mater.* **2** (1987) 512.

Received 23 November 1993
and accepted 7 June 1993